remote sensing

MDPI

Article

Wind Direction Signatures in GNSS-R Observables from Space

Dongliang Guan [1,2,*], Hyuk Park [3], Adriano Camps [3,*], Yong Wang [1,2], Raul Onrubia [3], Jorge Querol [3] and Daniel Pascual [3]

1 State Key Laboratory of Geodesy and Earth's Dynamics, Institute of Geodesy and Geophysics, Chinese Academy of Sciences, Wuhan 430077, China; ywang@whigg.ac.cn
2 University of Chinese Academy of Sciences, Beijing 101408, China
3 Department of Signal Theory and Communications, University Politecnica de Catalunya, and IEEC/CTE-UPC, 08034 Barcelona, Spain; park.hyuk@tsc.upc.edu (H.P.); onrubia@tsc.upc.edu (R.O.); jorge.querol@tsc.upc.edu (J.Q.); daniel.pascual@tsc.upc.edu (D.P.)
* Correspondence: guandongliang@whigg.ac.cn (D.G.); camps@tsc.upc.edu (A.C.)

Received: 7 December 2017; Accepted: 25 January 2018; Published: 29 January 2018

Abstract: Wind speed and direction are important essential climate variables (ECVs). GNSS-R is an emerging remote sensing technique that can be potentially used to retrieve wind speed from space. However, few studies have addressed the wind direction retrieval from spaceborne GNSS-R observables, namely the Delay Doppler map (DDM). In this study, the feasibility of retrieving wind direction from the synthetic DDMs is analyzed. First, the simulation tool P^2EPS is used to generate the DDMs under different geometry configurations, wind speed, and wind direction. Then, DDM changes caused by the wind direction are investigated, and two metrics are proposed to retrieve the wind direction from the DDM shape changes. The influence on wind direction retrieval of the wind speed, receiver's elevation, and azimuth is further discussed. Finally, the sensitivity of DDM changes to noise is investigated, as well as the impact of noise on these two metrics.

Keywords: global navigation satellite system-reflectometry (GNSS-R); Delay-Doppler-Map (DDM); wind direction

1. Introduction

Wind speed and direction are important essential climate variables (ECVs). Wind speed and direction drive the air-sea interaction and have an impact on the ocean's surface, the evaporation rate, the mixing of surface waters, and the development of seiches and storm surges. At present, wind vector is routinely measured by passive and active microwave instruments.

Microwave radiometers measure the changes in the emissivity due to the ocean surface roughness, which is correlated to the wind speed above the water's surface. Microwave polarimetric radiometers can also measure both the wind speed and the wind direction by making use of the third Stokes parameter (the fourth one being nearly negligible). Coriolis WindSat [1] is the first satellite mission carrying a microwave polarimetric radiometer. The spatial resolution is determined by the antenna footprint, and the typical resolution is about 25 km.

Scatterometers are active microwave instruments. They send an electromagnetic signal toward the Earth's surface, which then reflects them through a Bragg scattering mechanism of the surface capillary waves present over the large scale ocean waves. The reflected energy measured by the scatterometer at different azimuthal angles is then translated using a geophysical model function (GMF) into a 10 m neutral wind speed and direction. Scatterometers typically operate at either C-band (~5 GHz) or Ku-band (~14 GHz). Sample scatterometers that have been in operation are ERS-1/2 (C-band), QuikScat (Ku-band), and ASCAT (C-band) on Envisat, and the spatial resolution is about 12 km.

Spaceborne Global Navigation Satellite System (GNSS) Reflectometry (GNSS-R) is a relatively new remote sensing technique that exploits opportunistically the GNSS signals reflected off the surface of the Earth in a forward bistatic configuration. There are numerous GNSS satellites transmitting in medium Earth orbits. On the other hand, the receiver is a passive instrument on board a low Earth orbit satellite. The first spaceborne experiment demonstrating GNSS-R, was the UK-DMC satellite which was launched in 2003. After the UK-DMC, several other GNSS-R satellites followed, including the UK TechDemoSat-1 (TDS-1) launched in 2014 [2], UPC's ^{3}Cat-2 satellite [3], and NASA's Cyclone Global Navigation Satellite System (CYGNSS) constellation [4] launched in 2016. Another opportunistic GNSS-R instrument turned to be the Soil Moisture Active Passive (SMAP) satellite launched in 2015, after the failure of its radar transmitter. On 20 August 2015, the SMAP radar receiver was tuned to 1227.45 MHz to collect GPS L2C signals [5,6]. These spaceborne GNSS-R missions have explored various applications of GNSS-R techniques: ocean altimetry [7–9], ocean scatterometry [10–16], sea ice [7,8,17–19], oil spills detection [20], soil moisture and vegetation [21,22], and ionosphere [23]. As compared to the traditional spaceborne instruments measuring ocean wind, GNSS-R has weaker received signals and requires longer integration times, but it has its own advantages as well. It is relatively cheap to deploy a constellations of small satellites, because the instrument is a passive GNSS-R receiver with low mass, low power, and low cost, and the expensive and larger transmitters are the already GNSS satellites operating in orbit. By 2020, when the GPS, GLONASS, Galileo, and Beidou will be fully operational, more than 100 transmitting satellites will be in orbit, which will provide short revisit times and improved surface sampling, making real-time ocean monitoring possible.

The retrieval of ocean wind speed from spaceborne GNSS-R observation has already been widely discussed, and it is well developed [11,12,14,24–30]. However, few studies have focused on wind direction. Garrison [31] fitted the aircraft measured waveforms to a geometric optics based model using the directional mean square slopes. Zuffada et al. [32] analyzed the behavior of the trailing edge of the reflected GPS signal waveforms to determine the wind direction. The impact of the reflection geometry, coherence time, and the receiver integration time on wind direction retrieval were also discussed. Komjathy et al. [33] also retrieved ocean surface wind speed and wind direction using reflected GPS signals. Valencia et al. [34] used DDM asymmetry metrics to retrieve the wind direction in an airborne experiment. Zavorotny and Voronovich [35] studied the sensitivity of the modeled bistatic radar cross-section to wind direction, and found that bistatic scattering exhibits a sensitivity to wind direction when the scattering direction does not coincide with the nominal specular direction. Similarly Park et al. [36,37] used the normalized radar cross-section (NRCS) to study wind direction effects on sea surface specular scattering for GNSS-R applications. For a purely specular geometry, variations of the NRCS are too small to sense wind direction. For slightly non-specular geometries, larger variations with wind direction can be found at individual surface points.

All the above studies of wind direction either focused on reflected GPS-R airborne measurements [31–34] or its effects on the GNSS-R radar cross-section [35–37]. In this study, the possibility to retrieve wind direction from spaceborne GNSS-R observables is investigated. First, Delay-Doppler maps (DDMs) are simulated for a scenario similar to the UK TDS-1 one. Second, the influence of the wind direction on the DDM is investigated by computing the difference of the DDMs simulated under different wind directions. Then, two metrics are proposed to relate the DDM asymmetry to the wind direction. The impact on the two metrics of the wind speed, receiver's elevation, and azimuth is further investigated. Finally, the sensitivity of the DDM changes caused by wind direction is discussed under the presence of noise, as well as the impact of noise on the two metrics.

2. Methodology

2.1. Theoretical Background of Wind Speed Retrieval from the DDM

The most complete observable from a spaceborne GNSS-R receiver is the Delay-Doppler map (DDM), which is obtained as the cross-correlation of the received scattered GPS signal with a locally

generated replica of the transmitter GPS signal over a range of delay offsets and Doppler shifts. Zavorotny and Voronovich [38] developed a theoretical scattering model for the bistatically reflected GPS signals based on the geometric optics limit of the Kirchhoff approximation, which describes the power of reflected GPS signal as a function of geometry and environment parameters. The DDM over the sea surface is modelled as

$$\langle |Y_r(\tau, f)|^2 \rangle = \frac{P_T \lambda^2 T_i^2}{(4\pi)^3} \iint\limits_{A_s} \frac{G_T(\vec{\rho}) G_R(\vec{\rho}) \left| \chi^2(\delta_\tau, \delta_f) \right|^2}{R_T^2(\vec{\rho}) R_R^2(\vec{\rho})} \sigma_{pq}^0(\vec{\rho}) d^2\vec{\rho}, \tag{1}$$

where P_T and $G_T(\vec{\rho})$ represent the satellite transmitted power and antenna gain, respectively, λ is the electromagnetic wavelength of the signal, $G_R(\vec{\rho})$ is the receiving antenna gain, $R_T(\vec{\rho})$ and $R_R(\vec{\rho})$ are the distances between the surface point $\vec{\rho}$ and the transmitter and receiver, respectively, and $\sigma_{pq}^0(\vec{\rho})$ is the polarization-dependent bi-static radar scattering coefficient, or simply scattering coefficient. χ is the Woodward Ambiguity Function (WAF) [39], which accounts for the signal modulation characteristics. The integration domain A_s is referred to as the "glistening zone," which is the active scattering area that effectively contributes to the reflected signal. The DDM $\langle |Y_r(\tau, f)|^2 \rangle$ corresponds to the GNSS power scattered by the surface as a function of the delay τ and Doppler frequency f. Due to the spatial filtering of the WAF, the DDM points can be related to the contributions from cells on the surface, which correspond to the intersection of the iso-delay and iso-Doppler lines.

In Equation (1), the parameter dependent on the wind direction is the scattering coefficient, which is usually modelled using the Kirchhoff model under the geometric optics approximation

$$\sigma_{pq}^0(\vec{\rho}) = \frac{\pi |\mathcal{R}|^2 q^4}{q_z^4} P(\vec{s}), \tag{2}$$

where $\mathcal{R}$ is the Fresnel reflection coefficient, and $\vec{q}$ is the scattering vector, $\vec{s} = -\frac{\vec{q}_\perp}{q_z} = (s_u, s_c)$ is the sea surface slope vector, where s_u and s_c denote the surface slope components to the up-wind and cross-wind direction, respectively. The wind speed and direction contribution appear in the sea surface slope probability density function (PDF) $P(\vec{s})$.

In [38], the sea surface slope PDF is modelled using a Gram–Charlier distribution, which is function of mean-square-slope (MSS) of up-wind mss_u and cross-wind mss_c [40].

$$P(s_u, s_c) = \left[\frac{1}{2\pi \sqrt{mss_u \cdot mss_c}} \exp\left\{ -\frac{1}{2} \left(\frac{s_u^2}{mss_u} + \frac{s_c^2}{mss_c} \right) \right\} \right] \left[1 + \sum_{i,j=1}^{\infty} c_{ij} H_i(s_u) H_j(s_c) \right], \tag{3}$$

where H_i and H_j are Hermite polynomials with coefficient c_{ij}. The details of Equation (3) are described in [40] and further elaborated one is in [41].

The first order Gram-Charlier distribution is equivalent to the Gaussian function with semi-major axis mss_u and semi-minor axis mss_c. The Gram–Charlier distribution introduces the skewness and peakedness in the sea surface slope PDF. Therefore, the scattering coefficients show the specific features corresponding to the wind direction. The up-wind direction coincides with semi-major axis of the scattering coefficient distribution, and the peak shifts to the up-wind direction.

Figure 1 shows sample scattering coefficient distributions for different wind speeds and directions, computed under the conditions of the UK TDS-1 scenario. For the simulation study, the sea surface slope PDF $P(\vec{s})$ is generated using Equation (3) on the (s_u, s_c) domain. Then, the $P(\vec{s})$ is mapped (rotated) on the X-Y domain such that up-wind direction s_u coincide with the wind direction on the X-Y domain.

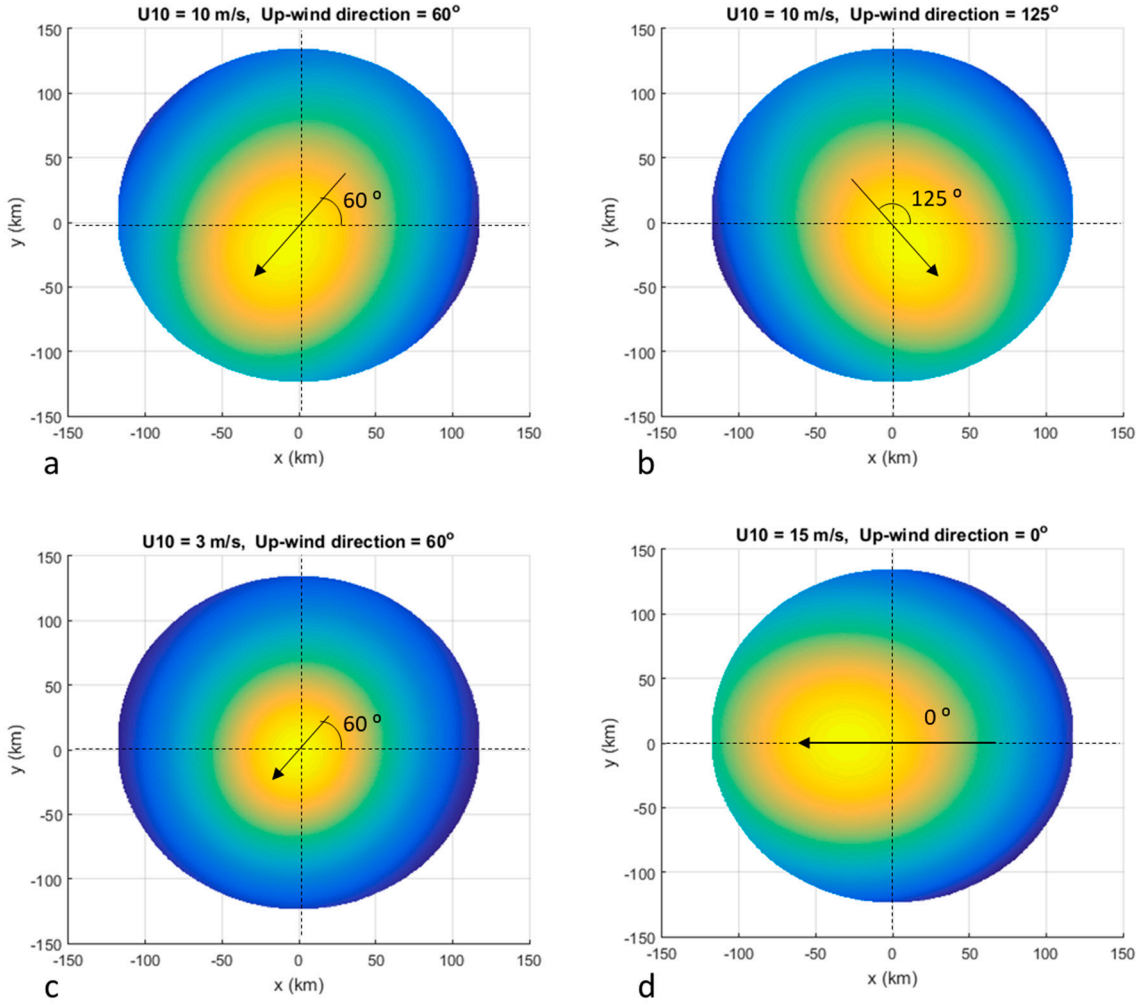

Figure 1. Scattering coefficients over the glistening zone with various wind speed and direction: (**a**) 10 m/s with 60°, (**b**) 10 m/s with 125°, (**c**) 3 m/s with 60°, and (**d**) 15 m/s with 0°.

Comparing Figure 1a,b, the up-wind directions are along with semi major-axis. Comparing Figure 1a, 1b, and 1d, the shifts of peak are also along the up-wind direction (semi-major axis), and magnitude of the shift is roughly proportional to the wind direction. These features illustrate well the PDF of the sea surface slope modelled by the Gram-Charlier distribution. The variability of the scattering coefficient with regard to the wind direction transfers into the DDM shape, which should allow to perform the wind direction retrieval from spaceborne GNSS-R measurements.

2.2. Simulation Studies

The simulator tool PAU/PARIS End-to-end Performance Simulator (P^2EPS) [42,43] used in this study is based on the scattering model described in Section 2.1. The observation geometry for the simulation is illustrated in Figure 2. The details of scattering reference frame definition of P^2EPS are described in [44].

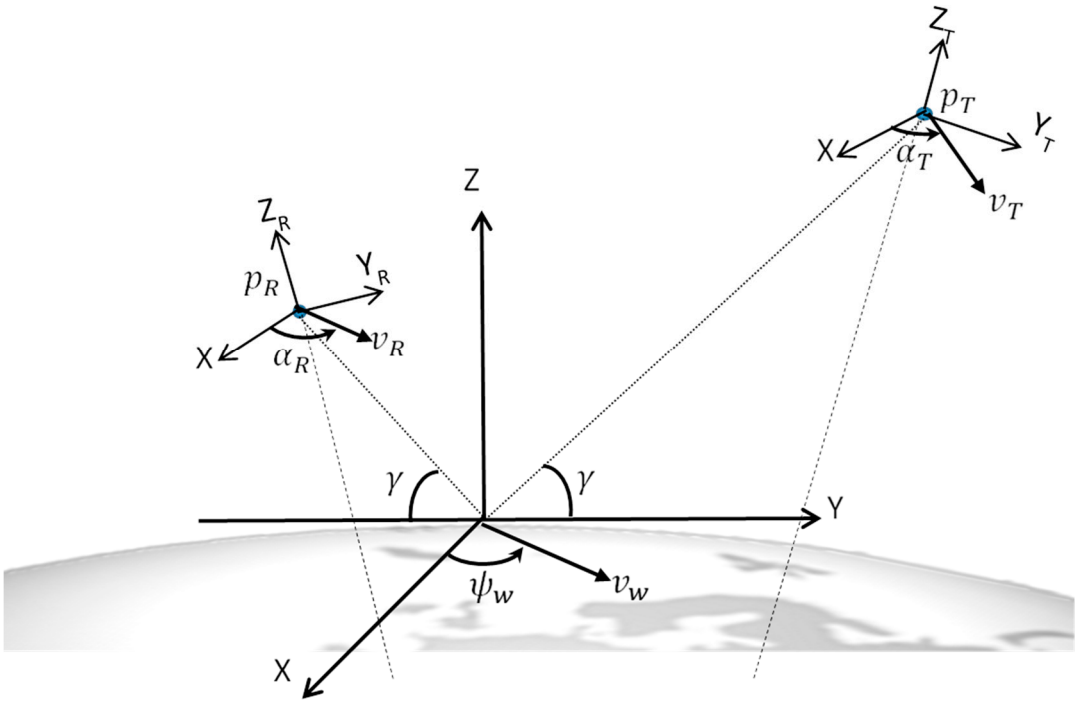

Figure 2. Definition of scattering reference frame (SRF) for simulation. The up-wind direction is defined by azimuth angle ψ_w, the moving directions of transmitter and receiver satellite are denoted by azimuth angles α_T and α_R, respectively. More details of SRF are described in in [44].

There are several parameters that have to be considered: the altitude, the azimuths (α_R and α_T), and the elevation angle (γ) of the receiver and transmitter, and the wind speed ($|v_w|$) and direction (ψ_w). The first three parameters describe mainly the geometry of the scattering scenario, and the last two determine the status of the ocean surface, from which the directional mean square slope of the ocean surface can be computed.

In the simulations, the scenario of UK TDS-1 has been chosen, i.e., the altitude of the receiver is set to 625 km, and the coherent and incoherent integration time is set to 1 and 1000 msec, respectively. At this orbital height, the satellite speed is about 7.55 km/s. To examine the influence of wind direction, the wind direction ψ_w is set from 0° to 360° in steps of 30°. Meanwhile, the influence of other parameters on wind direction retrieval is also investigated. The azimuth of the receiver α_R and transmitter α_T is set from 0° to 360° in steps of 30°. The elevation angle γ is set to 60°, 65°, 75°, and 85°. The wind speed ($|v_w|$) is set to 5, 10, 15, 20, and 25 m/s. The DDMs are then simulated under the different combinations of the mentioned parameters, including speckle and thermal noises to mimic the real scenes [42,43]. After the generation of the DDMs, the noise-free DDM for a wind direction of 0° is subtracted from the noise-free DDMs to investigate the shape and power changes of DDMs caused by the wind direction.

According to the GNSS-R bistatic radar equation, wind direction causes the directional variations of ocean surface slope, and these variations result in the DDM asymmetry. Therefore, two metrics are proposed according to the DDM asymmetry to establish the relation with wind direction. The first metric is chosen as the azimuth of the vector pointing from the origin (O) of DDM to the CM, namely angle φ_1 in Figure 3. This origin corresponds to the specular point, where both code delay and Doppler shifts are zero ($\delta_\tau = 0,\ f_\rho = 0$). The second metric is proposed by Valencia et al. [34] defined as the azimuth of the vector pointing from the center of mass of the DDM (CM) to the center of mass of the DDM skirt (CM_{skirt}), namely angle φ_2 in Figure 3. The DDM skirt is a region whose power is within a certain ratio to the DDM peak, which is more sensitive to the wind direction than the area around the specular point. In Figure 3, the DDM skirt is defined as the region whose power is within 30% and

70% to the peak. In this study, various ranges of DDM skirt are tested to identify its influence on the wind direction retrieval. When calculating the two metrics, the DDM power is normalized to the peak of DDM to avoid any calibration issues.

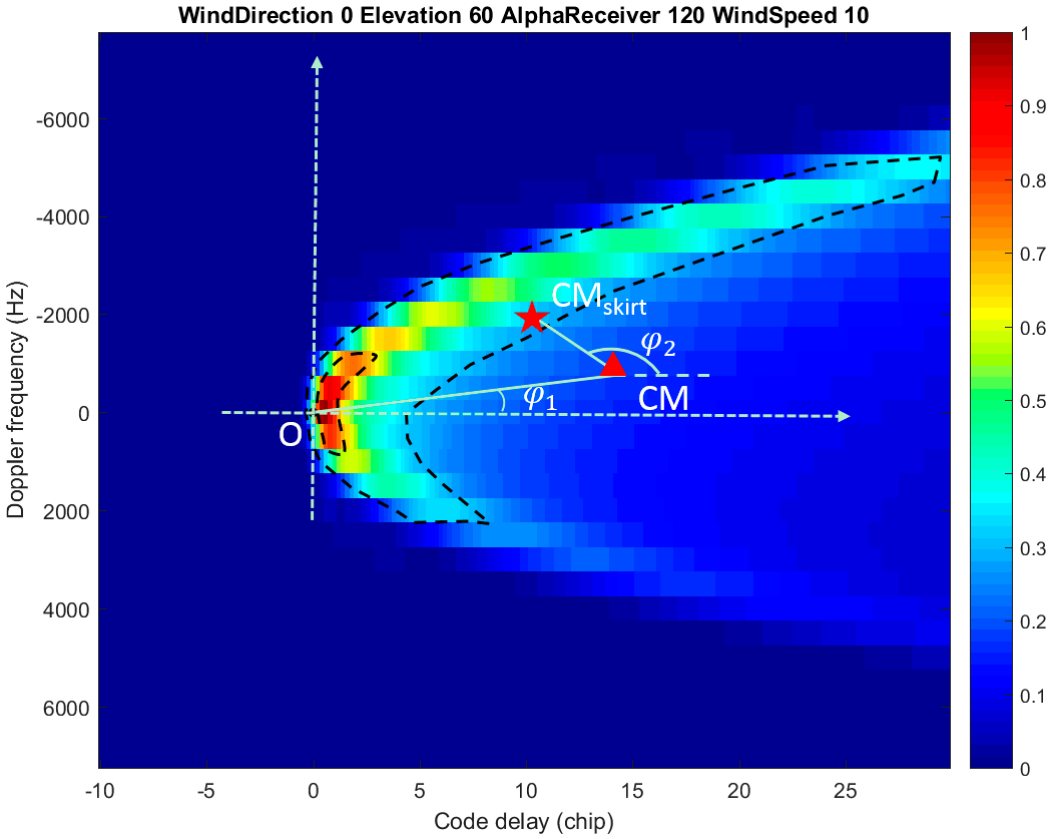

Figure 3. Definition of two metrics: (1) φ_1, the azimuth of vector pointing from the specular point to the center of mass (CM, red triangle); (2) φ_2, the azimuth of vector pointing from the center mas (CM) to center of mass of Delay Doppler map (DDM) skirt (CM_{skirt}, red pentagram). The DDM is simulated under wind direction 0°, elevation 60°, azimuth 120°, and wind speed 10 m/s, and is normalized to the peak of DDM. The region surrounded by the black dash lines is the DDM skirt, whose normalized power ranges from 0.3 to 0.7.

To study the sensitivity of DDM changes caused by the wind direction to the noise, the modeled DDMs for different noise levels are differentiated. Meanwhile, the two metrics φ_1 and φ_2 are computed from the DDMs for different noise levels in order to figure out the influence of noise on the wind direction retrieval. Then, they are compared to those derived from noise-free DDMs. The root-mean-square error (RMSE) of the angles φ_1 and φ_2 are computed, as well as the ratios of the RMSE to the amplitude of the two metrics' oscillations. This allows us to find the required signal-to-noise ratio (SNR) for the spaceborne observables and ultimately the antenna directivity.

3. Results and Discussion

3.1. DDM Variations Caused by Wind Direction Changes

The DDM variations caused by the changes of wind direction are examined first. Figure 4a–c shows the simulation results of DDM in which wind speed, elevation, and azimuth of the receiver are 10 m/s, 60°, and 30°. The wind direction of Figure 4a–c are 0°, 30°, and 120°.

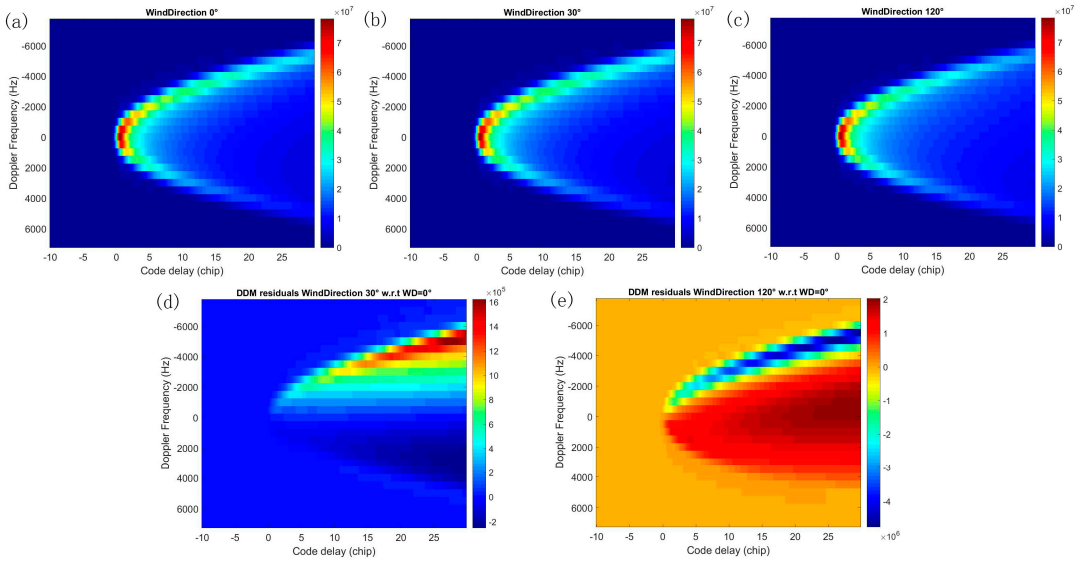

Figure 4. DDM simulations under different wind direction (**a**) 0°; (**b**) 30°; (**c**) 120°. DDM differences w.r.t. the DDM of wind direction 0°. (**d**) The DDM residual of wind direction of 30°; (**e**) The DDM residual of wind direction of 120°. The wind speed, elevation and azimuth of the receiver are 10 m/s, 60°, and 30°.

To illustrate the differences caused by the wind direction, the DDMs simulated for wind directions of 30° and 120° are compared to the DDM of wind direction of 0°. As shown in Figure 4d,e, the variations caused by the wind direction are located in the "horseshoe" of the DDM. For both cases, the upper "horseshoe" has larger differences than the lower part. Wind directions of 30° and 120° have different variations with regard to the wind direction of 0°. Wind direction of 120° causes larger differences than that of wind direction of 30°. The value of DDM here is represented by using the arbitrary linear unit for power, which is equivalent to the un-calibrated power.

Two metrics are calculated for each DDM simulation with different wind directions. Figures 5–8 show the behavior of these two metrics as a function of the wind direction. A near sinusoidal relation is found between these two metrics and wind direction. However, other parameters also affect this relationship.

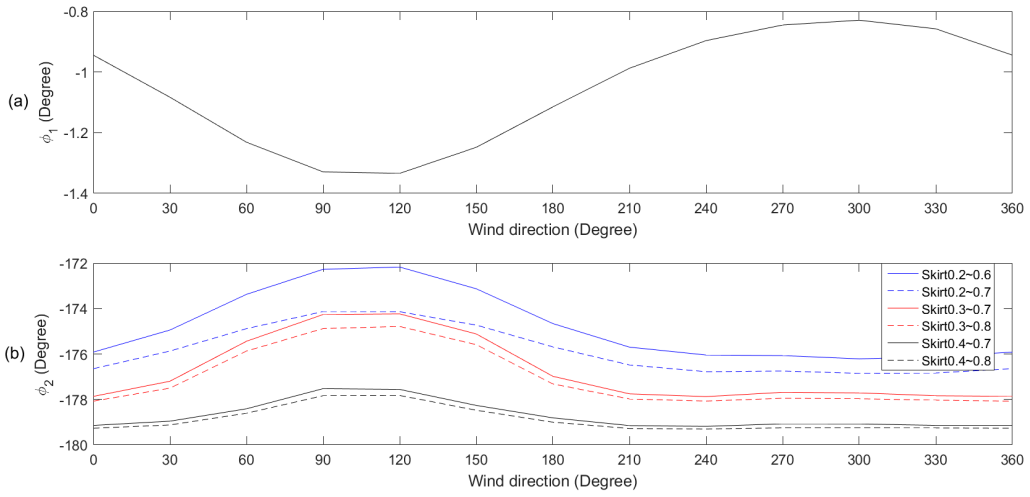

Figure 5. The influence of the DDM skirt's value on the relation between wind direction and the angles of (**a**) φ_1 and (**b**) φ_2. The wind speed, the receiver's elevation, and azimuth are 10 m/s, 75°, and 108°.

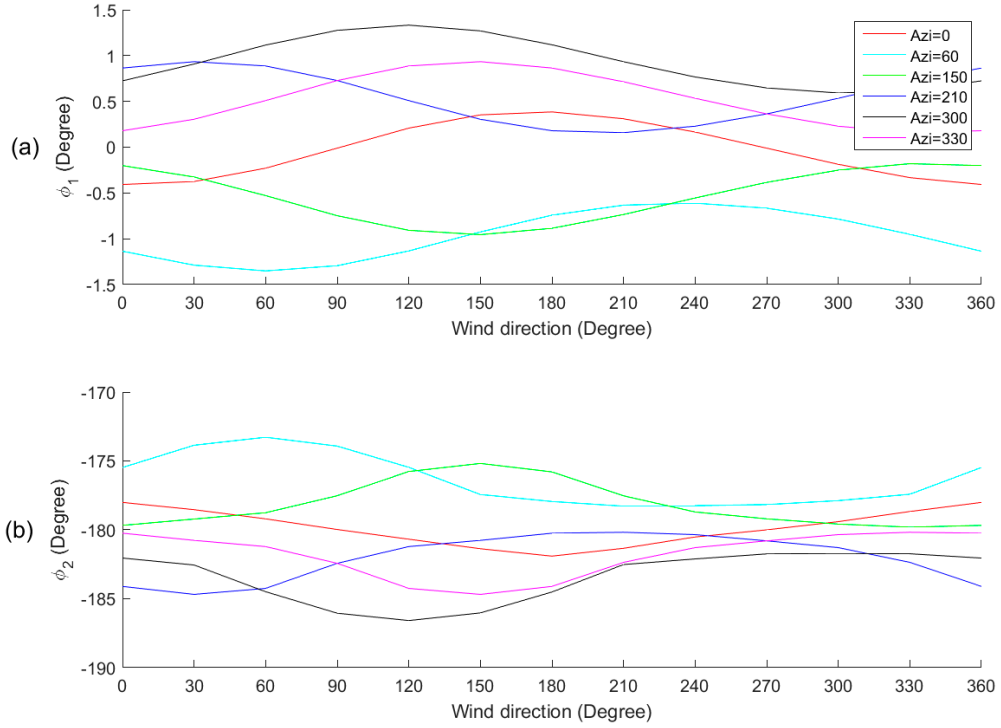

Figure 6. The influence of the receiver's azimuth on the relation between wind direction and the angles of (**a**) φ_1 and (**b**) φ_2. The wind speed and the receiver's elevation are 15 m/s and 75°.

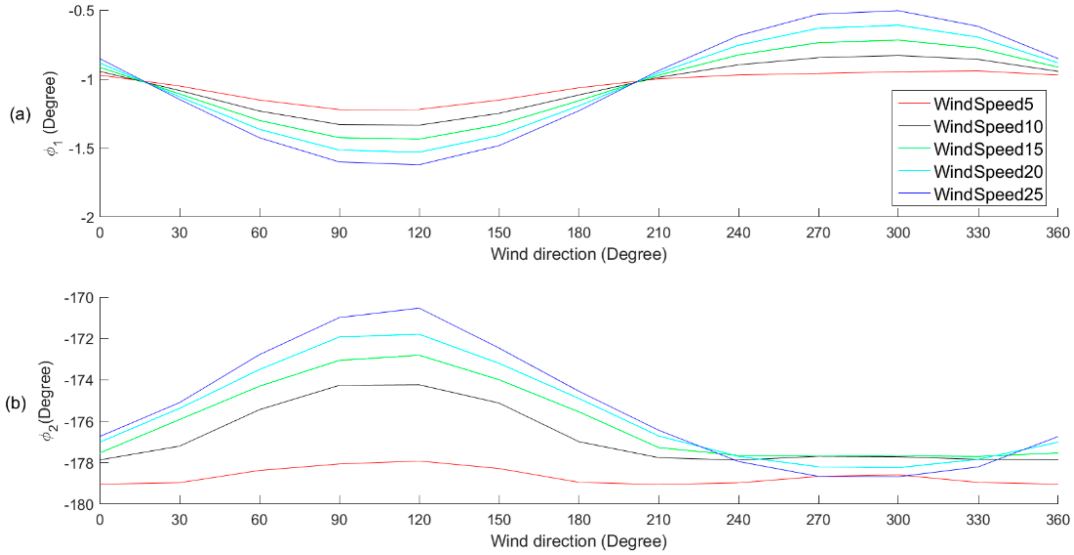

Figure 7. The influence of wind speed on the relation between wind direction and the angles of (**a**) φ_1 and (**b**) φ_2. The elevation and azimuth of the receiver are 75° and 108°.

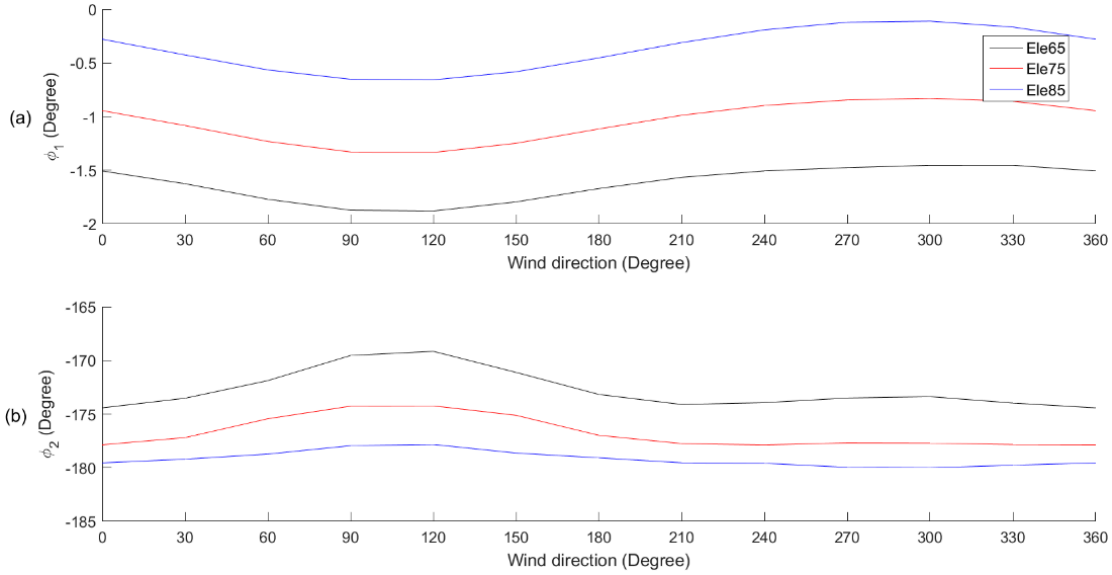

Figure 8. The influence of elevation of the receiver on the relation between wind direction and the angles of (**a**) φ_1 and (**b**) φ_2. The wind speed and receiver's azimuth are 10 m/s and 108°.

Figure 5 shows the influence of the DDM skirt value defined w.r.t. the peak value of the DDM. Metric φ_1 is independent of the choice of DDM skirt value. Different ranges of DDM skirt values affect the relation between the wind direction and the angle of CM-CM_{skirt} (φ_2). The maximum skirt value (0.6, 0.7, or 0.8) has little effect on the relation, and only causes minor drifts. On the other hand, the minimum skirt value (0.2, 0.3, or 0.4) causes relatively larger shifts because the variation of wind direction mainly affects the peripheral region of the DDM, the corresponding power of which is small. Besides, the smaller the minimum value of the skirt, the larger amplitude of the oscillations. However, as will be explained later, a relatively large minimum skirt value is preferable because it is more robust in front of noise. Even though different ranges of skirt values cause shift and amplitude changes of the oscillation, the basic shape is nearly the same.

The azimuth of the receiver has also a great influence on the wind direction retrieval because the receiver's azimuth variations result in different geometrical configurations of the transmitter, receiver, and reflecting surface, which affect the DDM. A series of different azimuth values have been simulated to investigate its influence on the two metrics, as shown in Figure 6. Different azimuths have their corresponding relation curves, which would have to be taken into account in any wind direction retrieval algorithm. On the other hand, according to the simulations, the influence of transmitter's azimuth is negligible, only accounting about 1% of the influence of the receiver's azimuth. It is because the transmitter (altitude ~20,200 km) is far from the reflected surface as compared to the receiver (altitude ~625 km).

Figure 7 shows the impact of wind speed. For both metrics, as the wind speed increases, the amplitude of the oscillation also increases because the glistening zone is enlarged, and therefore the reflected power from the peripheral part also increases. Despite the amplitude variations caused by the wind speed, the basic shape of the oscillations remains the same for the angle φ_1.

At last, the effect of the elevation of the receiver is investigated. As shown in Figure 8, for the angle φ_1, the oscillations are nearly the same despite the shifts between them. For the angle φ_2, the elevation change causes both a bias and an amplitude change of the oscillations. The lower the elevation, the larger the amplitude and vice-versa. In both cases, the vectors CM-Origin (φ_1) and CM_{skirt}-CM (φ_2) are closer to the horizontal axis for larger elevations, since when elevation increases, the horseshoe shape of the DDM becomes more symmetrical.

Both metrics suffer from the effect of wind speed, azimuth, and elevation of the receiver, which makes it difficult to build a unified Geophysical Model Function (GMF) that fits all situations. Instead, a look-up table (LUT) parameterized as a function of all geometry parameters seems more convenient, leaving only the wind speed and direction as free variables, as shown in Table 1. As compared to the angle CM_{skirt}-CM (φ_2), the angle CM-Origin (φ_1) is less affected by the above three parameters, and it is free from the effect of the DDM skirt. However, its amplitude is quite small (<1°), and therefore more difficult to measure.

Table 1. Look up table for wind speed and wind direction retrieval.

Azimuth (°)	Elevation (°)	φ_2 (°)	φ_1 (°)	Wind Speed (m/s)	Wind Direction(°)
108	65	−173.52	−1.63	10	30
108	65	−169.15	−1.88	10	120
108	75	−175.44	−1.23	10	60
108	75	−173.50	−1.36	20	60
108	85	−177.73	−0.67	15	150
30	75	−179.81	−0.18	15	210
60	75	−173.92	−1.29	15	90

3.2. Effect of Noise

A series of simulations for different SNR were performed from 1 dB to 15 dB in steps of 2 dB. The definition of the SNR is the same as the one used for UK TDS-1 [45].

$$\mathrm{SNR} = 10 \cdot \log_{10}\left(\frac{P-N}{N}\right), \tag{4}$$

where P is the maximum value of DDM and N is the background noise level.

The first column in Figure 9 shows the DDM residuals for a wind direction of 30°, and the second one for 120° with regard to the wind direction of 0°. From top to bottom, the SNRs are 5 dB, 7 dB, 9 dB, 11 dB, and 13 dB, respectively. When the SNR equals 5 dB (Figure 9a,b), for a wind direction of 30°, the differences caused by the wind direction are masked by the noise. However, for a wind direction of 120°, the differences in the upper "horseshoe" can still be seen, although they still suffer from the high noise level. As the SNR increases, both differences become increasingly clear. When the SNR reaches to 11 dB (Figure 9g,h), the differences caused by a wind direction of 30° can be clearly identified from the background noise. For a wind direction of 120°, even the smallest differences in the lower part of the "horseshoe" can be seen. The different sensitivities of these two wind directions to SNR result from the power differences of these two directions. It is obvious that the larger power difference of wind direction of 120° is more resilient to the noise than the relatively smaller power difference of wind direction of 30°.

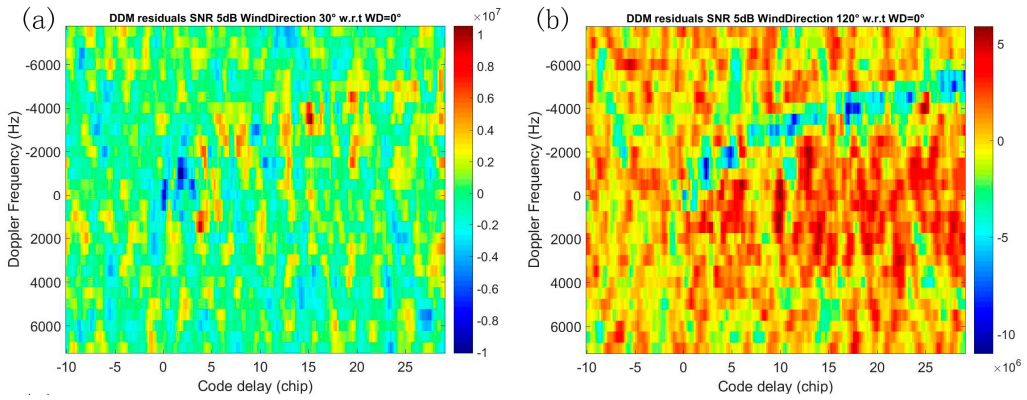

Figure 9. *Cont.*

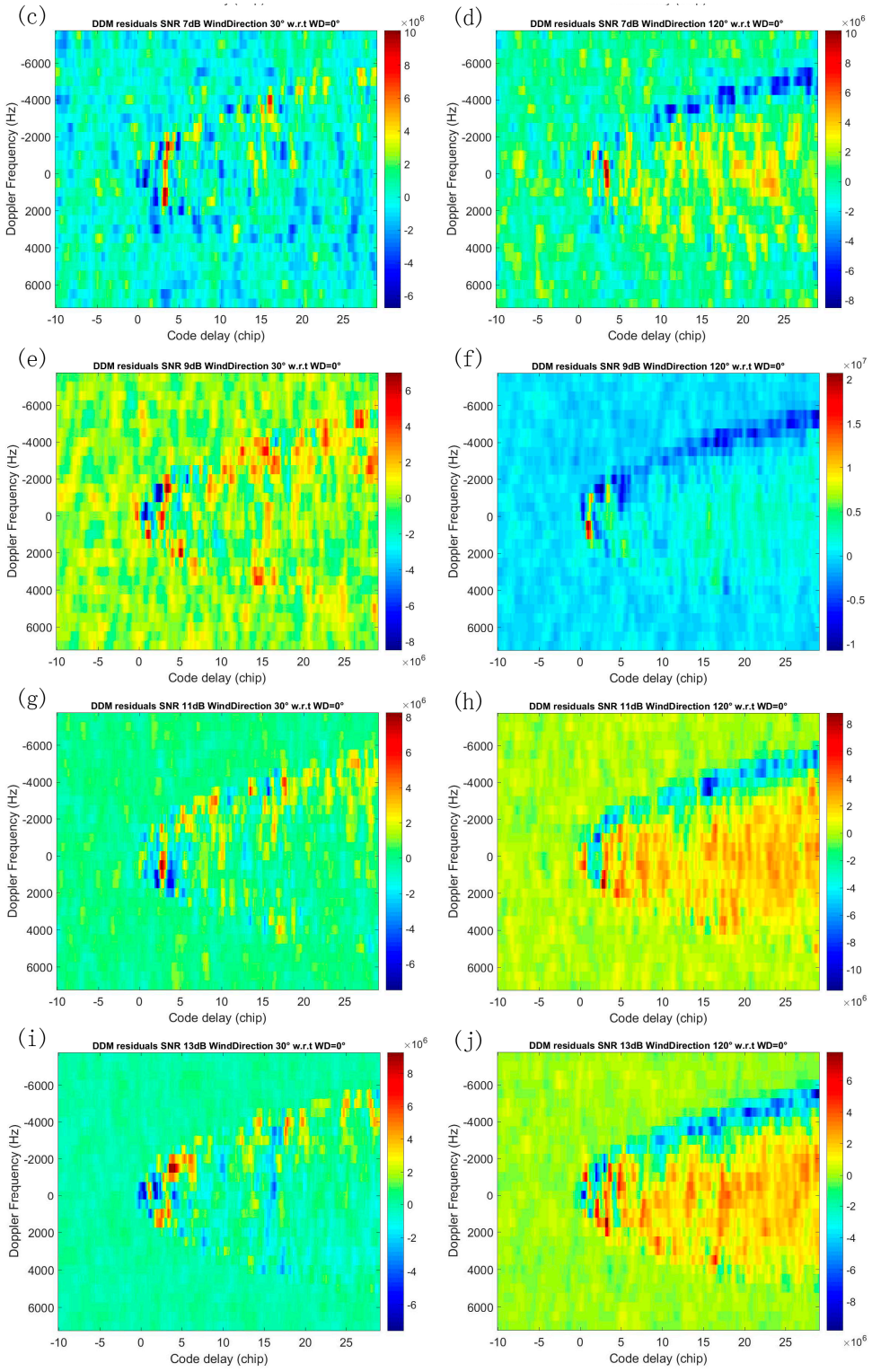

Figure 9. Noise DDM residuals with regard to DDM of wind direction 0°. The first column is DDM residuals of wind direction 30°, and the second column is DDM residuals of wind direction of 120°. From top to bottom, the SNR of each row is 5 dB, 7 dB, 9 dB, 11 dB, and 13 dB. (**a**) 30°, 5 dB; (**b**) 120°, 5 dB; (**c**) 30°, 7 dB; (**d**) 120°, 7 dB; (**e**) 30°, 9 dB; (**f**) 120°, 9 dB; (**g**) 30°, 11 dB; (**h**) 120°, 11 dB; (**i**) 30°, 13 dB; (**j**) 120°, 13 dB. The wind speed, elevation and azimuth of the receiver are 10 m/s, 60°, and 30°.

The two metrics φ_1 and φ_2 are now computed from the modeled DDMs for different noise levels with SNR ranging from 1 dB to 15 dB in steps of 2 dB. The RMSE of the angles φ_1 and φ_2 for each SNR are calculated w.r.t the two metrics derived from the noise-free DDMs, as well as the ratios of the RMSE to the corresponding amplitudes of the oscillations as shown in Figures 6–8.

Figure 10 shows the RMSE of the angles φ_1 and φ_2 with regard to the receiver's azimuth in Figure 6, and their corresponding ratios. For the angle φ_1, when SNR reaches to 11 dB, the RMSE is about 0.018°, and its ratio is about 7%. No significant improvement is observed from the SNR larger than 11 dB. For the angle φ_2, no obvious improvement of RMSE is observed when SNR reaches to 7 dB. However, its ratio is still high, about 40% on average. On the other hand, the receiver's azimuth change has more influence on the RMSE of angle φ_2 than that of the angle φ_1.

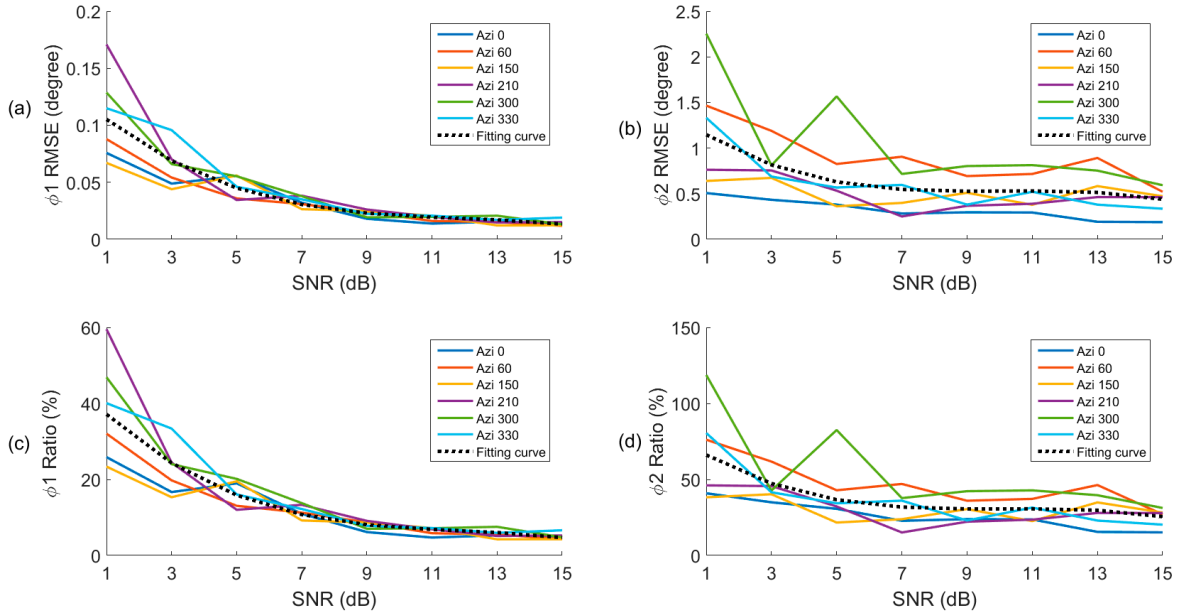

Figure 10. Root-mean-square error (RMSE) of angles (**a**) φ_1 and (**b**) φ_2 derived from DDMs with different SNRs and receiver's azimuths. The ratio of RMSE to the corresponding amplitude of the oscillation of angles (**c**) φ_1 and (**d**) φ_2.

Figure 11 shows the RMSE of the angles φ_1 and φ_2 with regard to the elevation angles in Figure 7 and their corresponding ratios. The RMSE and ratio of angle φ_1 is independent of the receiver's elevation, while the RMSE and ratio of angle φ_2 are affected by the receiver's elevation. Under the same SNR, the lower the receiver's elevation, the larger the RMSE and its ratio. When SNR reaches to about 11 dB, the RMSE and ratio of angle φ_1 are about 0.017° and 9%. For the angles φ_2, when SNR reaches to 11 dB, the RMSE and ratio also become nearly constant. However, the ratios of angles φ_2 are all considerably high, above 65% for an elevation of 65°, above 55% for an elevation of 75°, and above 40% for an elevation of 85°.

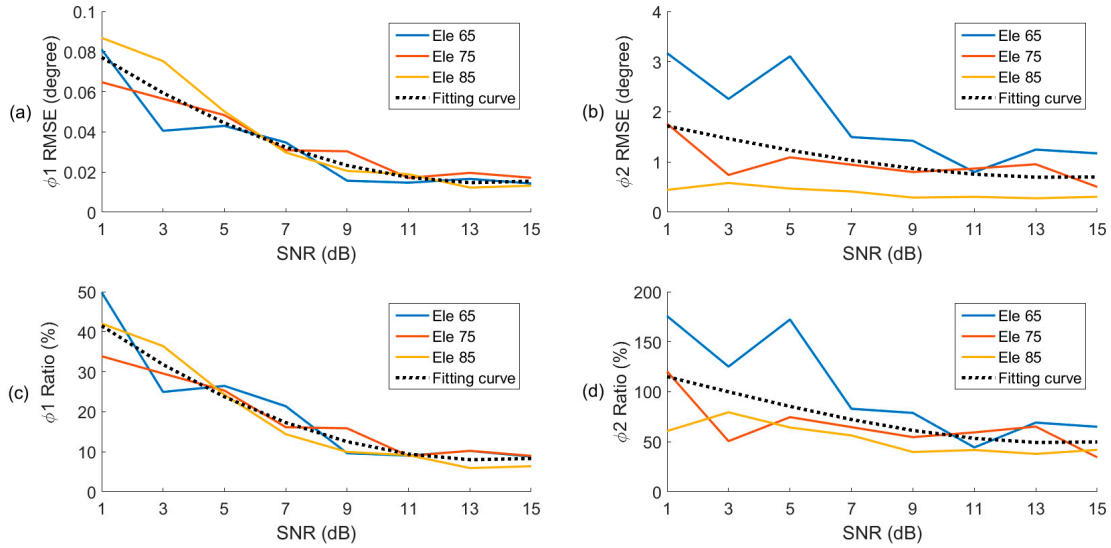

Figure 11. Root-mean-square error (RMSE) of angles (**a**) φ_1 and (**b**) φ_2 derived from DDMs with different SNRs and receiver's elevations. The ratio of RMSE to the corresponding amplitude of the oscillation of angles (**c**) φ_1 and (**d**) φ_2.

Figure 12 shows the RMSE of the angles φ_1 and φ_2 w.r.t the wind speed in Figure 8, and their corresponding ratios. Similar to the angle φ_1 in Figures 10 and 11, when SNR reaches to 11 dB, the RMSE and ratio are also about 0.017° and 8%. The RMSE and ratios of the angle φ_2 show opposite behavior. For the RMSE of angle φ_2, the larger the wind speed, the larger the RMSE. However, for the ratios of angle φ_2, when the wind speed is below 15 m/s, the larger the wind speed, the smaller the ratio. The average ratio of angle φ_2, except that of wind speed 5 m/s, is still high, above 40%.

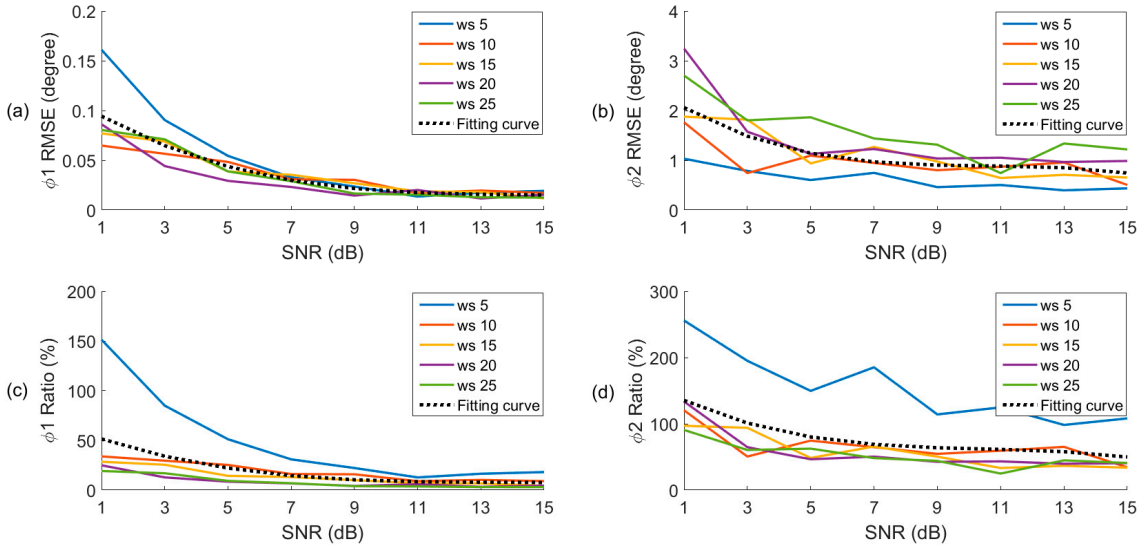

Figure 12. Root-mean-square error (RMSE) of angles (**a**) φ_1 and (**b**) φ_2 derived from DDMs with different SNRs and wind speeds. The ratio of RMSE to the corresponding amplitude of the oscillation of angles (**c**) φ_1 and (**d**) φ_2.

Simulation results show that the variations caused by the changes of wind direction can be detected. However, as the noise level increases, the DDM changes caused by the wind direction are gradually masked by the noise, which affects the retrieval of wind direction from two metrics. As the

SNR increases, the effects of noise on the angles φ_1 and φ_2 decrease. When SNR reaches to 11 dB, no more significant improvement can be seen with the further increase of SNR. As compared to the angle φ_2, the angle φ_1 is less affected by the noise and the changes of wind speed, receiver's azimuths, and elevations.

4. Conclusions

This study has theoretically investigated the possibility to retrieve wind direction from spaceborne GNSS-R observables. Simulation results show that the DDM changes caused by the wind direction can be detected. Two metrics, the angle CM-Origin (φ_1) and the angle CM_{skirt}-CM (φ_2), are used to establish the relation with wind direction. Both metrics reflect the wind direction, but both are also affected by other parameters. Wind speed causes the changes in the amplitude oscillations of both CM-Origin (φ_1) and CM_{skirt}-CM (φ_2). Receiver elevation angle causes the drift of CM-Origin (φ_1) oscillations and both drift and amplitude changes of CM_{skirt}-CM (φ_2) oscillations. Different azimuths have different curves for both metrics. It is difficult to find a unified function that fits all curves. Therefore, from an implementation point of view, a LUT will most likely have to be created, such as the one provided in Table 1. The influence of noise on wind direction retrieval from two metrics is also discussed. The metric angle φ_1 is more robust than the angle φ_2 with regard to noise. When SNR reaches to 11 dB, the ratio of RMSE to the amplitude of the oscillation of the angle φ_1 is only about 8%, while the ratio of angle φ_2 is above 40%. Therefore, in a real case study, GNSS-R observables of higher SNR (>11 dB) and the metric angle φ_1 are preferred in order to retrieve the wind direction.

Acknowledgments: This work was supported by the China National Key R&D Program (grant No. 2016YFB050 1700, 2016YFB0501705) and project "Técnicas avanzadas en teledetección aplicada usando señales GNSS y otras señales de oportunidad" (grant ESP 2015-70014-C2-1-R) from the Spanish MINISTERIO DE ECONOMIA Y COMPETITIVIDAD. Dongliang Guan received financial support from the China Scholarship Council.

Author Contributions: D.G. performed the simulations and analyzed the data; H.P. contributed to the simulator; A.C. proposed the idea for this study and revised the paper; D.C., H.P., A.C., Y.W., R.O, J.Q., and D.P. discussed the simulation results. D.G. and H.P. wrote the paper.

Conflicts of Interest: The authors declare no conflict of interest. The founding sponsors had no role in the design of the study; in the collection, analyses, or interpretation of data; in the writing of the manuscript, and in the decision to publish the results.

References

1. Gaiser, P.W.; St Germain, K.M.; Twarog, E.M.; Poe, G.A.; Purdy, W.; Richardson, D.; Grossman, W.; Jones, W.L.; Spencer, D.; Golba, G. The WindSat spaceborne polarimetric microwave radiometer: Sensor description and early orbit performance. *IEEE Trans. Geosci. Remote Sens.* **2004**, *42*, 2347–2361. [CrossRef]
2. Unwin, M.; Jales, P.; Tye, J.; Gommenginger, C.; Foti, G.; Rosello, J. Spaceborne GNSS-reflectometry on TechDemoSat-1: Early mission operations and exploitation. *IEEE J. Sel. Top. Appl. Earth Obs. Remote Sens.* **2016**, *9*, 4525–4539. [CrossRef]
3. Carreno-Luengo, H.; Camps, A.; Via, P.; Munoz, J.F.; Cortiella, A.; Vidal, D.; Jané, J.; Catarino, N.; Hagenfeldt, M.; Palomo, P. 3Cat-2—An Experimental Nanosatellite for GNSS-R Earth Observation: Mission Concept and Analysis. *IEEE J. Sel. Top. Appl. Earth Obs. Remote Sens.* **2016**, *9*, 4540–4551. [CrossRef]
4. Ruf, C.; Chang, P.; Clarizia, M.; Gleason, S.; Jelenak, Z.; Murray, J.; Morris, M.; Musko, S.; Posselt, D.; Provost, D. *CYGNSS Handbook*; Michigan Publishing: Ann Arbor, MI, USA, 2016.
5. Chew, C.; Lowe, S.; Parazoo, N.; Esterhuizen, S.; Oveisgharan, S.; Podest, E.; Zuffada, C.; Freedman, A. SMAP radar receiver measures land surface freeze/thaw state through capture of forward-scattered L-band signals. *Remote Sens. Environ.* **2017**, *198*, 333–344. [CrossRef]
6. Carreno-Luengo, H.; Lowe, S.; Zuffada, C.; Esterhuizen, S.; Oveisgharan, S. Spaceborne GNSS-R from the SMAP Mission: First Assessment of Polarimetric Scatterometry over Land and Cryosphere. *Remote Sens.* **2017**, *9*, 362. [CrossRef]
7. Clarizia, M.P.; Ruf, C.; Cipollini, P.; Zuffada, C. First spaceborne observation of sea surface height using GPS-Reflectometry. *Geophys. Res. Lett.* **2016**, *43*, 767–774. [CrossRef]

8. Hu, C.; Benson, C.; Rizos, C.; Qiao, L. Single-Pass Sub-Meter Space-Based GNSS-R Ice Altimetry: Results From TDS-1. *IEEE J. Sel. Top. Appl. Earth Obs. Remote Sens.* **2017**, *10*, 3782–3788. [CrossRef]
9. Rius, A.; Cardellach, E.; Fabra, F.; Li, W.; Ribó, S.; Hernández-Pajares, M. Feasibility of GNSS-R Ice Sheet Altimetry in Greenland Using TDS-1. *Remote Sens.* **2017**, *9*, 742. [CrossRef]
10. Clarizia, M.; Gommenginger, C.; Gleason, S.; Srokosz, M.; Galdi, C.; Di Bisceglie, M. Analysis of GNSS-R delay-Doppler maps from the UK-DMC satellite over the ocean. *Geophys. Res. Lett.* **2009**, *36*. [CrossRef]
11. Foti, G.; Gommenginger, C.; Jales, P.; Unwin, M.; Shaw, A.; Robertson, C.; Rosello, J. Spaceborne GNSS reflectometry for ocean winds: First results from the UK TechDemoSat-1 mission. *Geophys. Res. Lett.* **2015**, *42*, 5435–5441. [CrossRef]
12. Tye, J.; Jales, P.; Unwin, M.; Underwood, C. The first application of stare processing to retrieve mean square slope using the SGR-ReSI GNSS-R experiment on TDS-1. *IEEE J. Sel. Top. Appl. Earth Obs. Remote Sens.* **2016**, *9*, 4669–4677. [CrossRef]
13. Schiavulli, D.; Nunziata, F.; Migliaccio, M.; Frappart, F.; Ramilien, G.; Darrozes, J. Reconstruction of the radar image from actual DDMs collected by TechDemoSat-1 GNSS-R mission. *IEEE J. Sel. Top. Appl. Earth Obs. Remote Sens.* **2016**, *9*, 4700–4708. [CrossRef]
14. Clarizia, M.P.; Ruf, C.S. Bayesian Wind Speed Estimation Conditioned on Significant Wave Height for GNSS-R Ocean Observations. *J. Atmos. Ocean. Technol.* **2017**, *34*, 1193–1202. [CrossRef]
15. Valencia, E.; Camps, A.; Marchan-Hernandez, J.F.; Park, H.; Bosch-Lluis, X.; Rodriguez-Alvarez, N.; Ramos-Perez, I. Ocean surface's scattering coefficient retrieval by delay–Doppler map inversion. *IEEE Geosci. Remote Sens. Lett.* **2011**, *8*, 750–754. [CrossRef]
16. Park, H.; Valencia, E.; Rodriguez-Alvarez, N.; Bosch-Lluis, X.; Ramos-Perez, I.; Camps, A. New approach to sea surface wind retrieval from gnss-r measurements. In Proceedings of the 2011 IEEE International Geoscience and Remote Sensing Symposium (IGARSS), Vancouver, BC, Canada, 24–29 July 2011; IEEE: Piscataway, NJ, USA, 2011; pp. 1469–1472.
17. Yan, Q.; Huang, W. Spaceborne GNSS-R sea ice detection using Delay-Doppler Maps: First results from the UK TechDemoSat-1 mission. *IEEE J. Sel. Top. Appl. Earth Obs. Remote Sens.* **2016**, *9*, 4795–4801. [CrossRef]
18. Yan, Q.; Huang, W.; Moloney, C. Neural Networks Based Sea Ice Detection and Concentration Retrieval From GNSS-R Delay-Doppler Maps. *IEEE J. Sel. Top. Appl. Earth Obs. Remote Sens.* **2017**, *10*, 3789–3798. [CrossRef]
19. Alonso-Arroyo, A.; Zavorotny, V.U.; Camps, A. Sea Ice Detection Using UK TDS-1 GNSS-R Data. *IEEE Trans. Geosci. Remote Sens.* **2017**, *55*, 4989–5001. [CrossRef]
20. Valencia, E.; Camps, A.; Rodriguez-Alvarez, N.; Park, H.; Ramos-Perez, I. Using GNSS-R imaging of the ocean surface for oil slick detection. *IEEE J. Sel. Top. Appl. Earth Obs. Remote Sens.* **2013**, *6*, 217–223. [CrossRef]
21. Camps, A.; Park, H.; Pablos, M.; Foti, G.; Gommenginger, C.P.; Liu, P.-W.; Judge, J. Sensitivity of GNSS-R spaceborne observations to soil moisture and vegetation. *IEEE J. Sel. Top. Appl. Earth Obs. Remote Sens.* **2016**, *9*, 4730–4742. [CrossRef]
22. Chew, C.; Shah, R.; Zuffada, C.; Hajj, G.; Masters, D.; Mannucci, A.J. Demonstrating soil moisture remote sensing with observations from the UK TechDemoSat-1 satellite mission. *Geophys. Res. Lett.* **2016**, *43*, 3317–3324. [CrossRef]
23. Camps, A.; Park, H.; Foti, G.; Gommenginger, C. Ionospheric effects in GNSS-reflectometry from space. *IEEE J. Sel. Top. Appl. Earth Obs. Remote Sens.* **2016**, *9*, 5851–5861. [CrossRef]
24. Gleason, S. Space-based GNSS scatterometry: Ocean wind sensing using an empirically calibrated model. *IEEE Trans. Geosci. Remote Sens.* **2013**, *51*, 4853–4863. [CrossRef]
25. Li, C.; Huang, W. An algorithm for sea-surface wind field retrieval from GNSS-R delay-Doppler map. *IEEE Geosci. Remote Sens. Lett.* **2014**, *11*, 2110–2114.
26. Clarizia, M.P.; Ruf, C.S.; Jales, P.; Gommenginger, C. Spaceborne GNSS-R minimum variance wind speed estimator. *IEEE Trans. Geosci. Remote Sens.* **2014**, *52*, 6829–6843. [CrossRef]
27. Clarizia, M.P.; Ruf, C.S. Wind speed retrieval algorithm for the Cyclone Global Navigation Satellite System (CYGNSS) mission. *IEEE Trans. Geosci. Remote Sens.* **2016**, *54*, 4419–4432. [CrossRef]
28. Rodriguez-Alvarez, N.; Garrison, J.L. Generalized Linear Observables for Ocean Wind Retrieval from Calibrated GNSS-R Delay–Doppler Maps. *IEEE Trans. Geosci. Remote Sens.* **2016**, *54*, 1142–1155. [CrossRef]
29. Soisuvarn, S.; Jelenak, Z.; Said, F.; Chang, P.S.; Egido, A. The GNSS reflectometry response to the ocean surface winds and waves. *IEEE J. Sel. Top. Appl. Earth Obs. Remote Sens.* **2016**, *9*, 4678–4699. [CrossRef]

30. Giangregorio, G.; Addabbo, P.; Galdi, C. Wind retrieval for GNSS reflectometry from TechDemoSat-1. In Proceedings of the 2017 IEEE International Geoscience and Remote Sensing Symposium (IGARSS), Fort Worth, TX, USA, 23–28 July 2017; IEEE: Piscataway, NJ, USA, 2017; pp. 2667–2670.
31. Garrison, J.L. Anisotropy in reflected GPS measurements of ocean winds. In Proceedings of the 2003 IEEE International Geoscience and Remote Sensing Symposium, 2003, IGARSS'03, Toulouse, France, 21–25 July 2003; IEEE: Piscataway, NJ, USA, 2003; pp. 4480–4482.
32. Zuffada, C.; Elfouhaily, T.; Lowe, S. Sensitivity analysis of wind vector measurements from ocean reflected GPS signals. *Remote Sens. Environ.* **2003**, *88*, 341–350. [CrossRef]
33. Komjathy, A.; Armatys, M.; Masters, D.; Axelrad, P.; Zavorotny, V.; Katzberg, S. Retrieval of ocean surface wind speed and wind direction using reflected GPS signals. *J. Atmos. Ocean. Technol.* **2004**, *21*, 515–526. [CrossRef]
34. Valencia, E.; Zavorotny, V.U.; Akos, D.M.; Camps, A. Using DDM asymmetry metrics for wind direction retrieval from GPS ocean-scattered signals in airborne experiments. *IEEE Trans. Geosci. Remote Sens.* **2014**, *52*, 3924–3936. [CrossRef]
35. Zavorotny, V.U.; Voronovich, A.G. Recent progress on forward scattering modeling for GNSS reflectometry. In Proceedings of the 2014 IEEE International Geoscience and Remote Sensing Symposium (IGARSS), Quebec City, QC, Canada, 13–18 July 2014; IEEE: Piscataway, NJ, USA, 2014; pp. 3814–3817.
36. Park, J.; Johnson, J.T.; Ouellette, J. Modeling polarimetric sea surface specular scattering for GNSS-R applications. In Proceedings of the 2016 IEEE International Geoscience and Remote Sensing Symposium (IGARSS), Beijing, China, 10–15 July 2016; IEEE: Piscataway, NJ, USA, 2016; pp. 1903–1904.
37. Park, J.; Johnson, J.T. A Study of Wind Direction Effects on Sea Surface Specular Scattering for GNSS-R Applications. *IEEE J. Sel. Top. Appl. Earth Obs. Remote Sens.* **2017**, *10*, 4677–4685. [CrossRef]
38. Zavorotny, V.U.; Voronovich, A.G. Scattering of GPS signals from the ocean with wind remote sensing application. *IEEE Trans. Geosci. Remote Sens.* **2000**, *38*, 951–964. [CrossRef]
39. Skolnik, M.I. *Radar Handbook*; McGraw-Hill: New York, NY, USA, 1970.
40. Cox, C.; Munk, W. Measurement of the roughness of the sea surface from photographs of the sun's glitter. *JOSA* **1954**, *44*, 838–850. [CrossRef]
41. Wu, J. Mean square slopes of the wind-disturbed water surface, their magnitude, directionality, and composition. *Radio Sci.* **1990**, *25*, 37–48. [CrossRef]
42. Park, H.; Camps, A.; Pascual, D.; Kang, Y.; Onrubia, R.; Querol, J.; Alonso-Arroyo, A. A Generic Level 1 Simulator for Spaceborne GNSS-R Missions and Application to GEROS-ISS Ocean Reflectometry. *IEEE J. Sel. Top. Appl. Earth Obs. Remote Sens.* **2017**, *10*, 4645–4659. [CrossRef]
43. Park, H.; Camps, A.; Pascual, D.; Kang, Y.; Onrubia, R.; Querol, J. GARCA/GEROS-SIM M2 (Instrument to L1 module) Web Online Simulation Tool. Available online: http://rscl-grss.org/coderecord.php?id=474 (accessed on 12 January 2017).
44. Park, H.; Camps, A.; Valencia, E.; Rodriguez-Alvarez, N.; Bosch-Lluis, X.; Ramos-Perez, I.; Carreno-Luengo, H. Retracking considerations in spaceborne GNSS-R altimetry. *GPS Solut.* **2012**, *16*, 507–518. [CrossRef]
45. Foti, G.; Gommenginger, C.; Unwin, M.; Jales, P.; Tye, J.; Roselló, J. An assessment of non-geophysical effects in spaceborne GNSS Reflectometry data from the UK TechDemoSat-1 mission. *IEEE J. Sel. Top. Appl. Earth Obs. Remote Sens.* **2017**, *10*, 3418–3429. [CrossRef]